

Effective Methods for Human-Robot- Environment Interaction by means of Haptic Robotics

Pholchai Chotiprayanakul

A thesis submitted for the fulfilment
for the degree of
DOCTOR OF PHILOSOPHY

Faculty of Engineering and Information Technology
University of Technology, Sydney


March 2012

Declaration of Authorship

I, Pholchai Chotiprayanakul, certify that the thesis titled, “Effective Methods for Human-Robot-Environment Interaction by means of Haptic Robotics” and the work presented in this thesis are my own. I confirm that:

- This work was done while in candidature for the degree of doctor of philosophy at the University of Technology, Sydney.
- This thesis has not previously been submitted for a degree or any other qualification at any other institution.
- The thesis is based on work done by myself and where I have consulted the published work of others, this is always clearly attributed.
- All information sources and literature used are indicated in the thesis.

Signed:



Date:

21 / 03 / 12

Abstract

Industrial robots have been widely used to perform well-defined repetitive tasks in carefully constructed simple environments such as manufacturing factories. The futuristic vision of industrial robots is to operate in complex, unstructured and unknown (or partially known) environments, to assist human workers in undertaking hazardous tasks such as sandblasting in steel bridge maintenance. Autonomous operation of industrial robots in such environments is ideal, but semi-autonomous or manual operation with human interaction is a practical solution because it utilises human intelligence and experience combined with the power and accuracy of an industrial robot. To achieve the human interaction operation, there are several challenges that need to be addressed: environmental awareness, effective robot-environment interaction and human-robot interaction

This thesis aims to develop methodologies that enable natural and efficient Human-Robot-Environment Interaction (HREI) and apply them in a steel bridge maintenance robotic system. Three research issues are addressed: Robot-Environment-Interaction (REI), haptic device and robot interface and intuitive human-robot interaction.

To enable efficient robot-environment interaction, a potential field-based Virtual Force Field (VF^2) approach has been investigated. The VF^2 approach includes an Attractive Force (AF) method and a force control algorithm for robot motion control, and a 3D Virtual Force Field (3D- VF^2) method for real-time collision avoidance. Results obtained from simulation, experiments in a laboratory setup and field test have verified and validated these methods.

A haptic device-robot interface has been developed for providing intuitive human-robot interaction. Haptic devices are normally small compared to industrial robots. Thus, the workspace of a haptic device is much smaller than the workspace of a big industrial manipulator. A novel workspace mapping method, which includes drifting control, scaling control and edge motion control, has been investigated for mapping a

small haptic workspace to the large workspace of manipulator with the aim of providing natural kinesthetic feedback to an operator and smooth control of robot operation. A haptic force control approach has also been studied for transferring the virtual contact force (between the robot and the environment) and the inertia of the manipulator to the operator's hand through a force feedback function.

Human factors have significant effect on the performance of haptic-based human-robot interaction. An eXtended Hand Movement (XHM) model for eye-guided hand movement has been investigated in this thesis with the aim of providing natural and comfortable interaction between a human operator and a robot, and improving the operational performance. The model has been studied for increasing the speed of the manipulator while maintaining the control accuracy. This model is applied into a robotic system and it has been verified by various experiments.

These theoretical methods and algorithms have been successfully implemented in a steel bridge maintenance robotic system, and tested in both laboratory and a bridge maintenance site located in Sydney.

Acknowledgements

I would like to thank my supervisor Professor Dikai Liu for his great effort and time to advise and assist me throughout my candidature years. I also would like to thank my co-supervisor Professor Gamini Dissanayake for his support through my study. Without their support this thesis would not have been possible.

I would like to thank all my friends and colleagues at the ARC Centre of Excellence for Autonomous Systems (CAS), especially Dalong Wang, Ngai Ming Kwok, and Stephen Webb for their helpful comments and support. Special thanks to Gavin Paul, who gave a lot of helpful suggestions on improving the thesis.

Thanks to everyone at the Department of Industrial Engineering at King Mongkut's Institute of Technology Ladkrabang, especially Associate Professor Pornsak Auttavanich, Assistant Professor Sunpasit Limnorarath, and Associate Professor Rattikorn Varakulsiripun for giving me the best opportunity of my life.

Thanks to my sponsor, Ministry of Science and Thai Government for the scholarship and the Office of the Civil Service Commission (OCSC) and the Office of Educational Affairs in Australia for looking after me all years long of study.

Special thanks to my mum, my dad, and my family who have always supported and believed in me. Thanks to my wife "Sasima" and my daughter "Sasicha" for always being by my side and making me smile.

Table of Content

Declaration of Authorship.....	i
Abstract	ii
Acknowledgements	iv
List of Figures	x
Nomenclature	xix
Chapter 1 Introduction	1
1.1 Human-Robot-Environment Interaction: Research Challenges	1
1.2 The Targeted Application.....	4
1.3 Scope	6
1.4 Contributions.....	8
1.5 Publications	9
1.5.1 Conference Papers	9
1.5.2 Journal Papers	10
1.6 Thesis outline	10
Chapter 2 Literature Review	12
2.1 Human-Robot-Environment Interaction	13
2.2 Robot-Environment Interaction.....	14
2.2.1 Environmental Awareness	14
2.2.2 Collision-free Motion Planning	16
2.3 Human-Robot Interaction.....	21
2.3.1 Physical Human-Robot Interaction.....	22
2.3.2 Force Control Method.....	23

2.3.3	Safety in HRI	24
2.4	Haptic-based interaction.....	25
2.4.1	Haptic Force Reflection	26
2.4.2	Workspace Mapping	27
2.4.3	Computation Time and Time delay	28
2.5	Human Factors in Haptic Interface and Haptic-based Human-Robot Interaction	29
2.5.1	Fitts's Law	30
2.5.2	Steering Law	31
2.5.3	Control-Movement Scale and Control-Display Scale.....	32
2.5.4	Index of Performance.....	34
2.6	Summary	34
Chapter 3	Virtual Force Field Approach for Robot-Environment Interaction	36
3.1	Robot-Environment Interaction.....	37
3.2	Environmental Awareness.....	38
3.3	Extended Manipulator Model and Force Control Algorithm.....	39
3.3.1	Extended Manipulator Model	40
3.3.2	Force Control Algorithm.....	43
3.4	Attractive Force Method	46
3.4.1	Definition of Attractive Force.....	47
3.4.2	Attractive Force	50
3.5	Three-Dimensional Virtual Force Field Method.....	52
3.5.1	Ellipsoid Bounding	53
3.5.2	Swept Sphere Bounding.....	56
3.5.3	Constant E_r	59
3.6	Self-Collision Avoidance Method.....	60
3.6.1	Collision Detection Between Links of the Manipulator	60

3.6.2	Manipulator and Platform Collision Detection.....	62
3.7	Case Studies	63
3.7.1	Case Study 1: The 3D-VF ² Method for Collision Avoidance.....	64
3.7.2	Case Study 2: The VF ² Approach for Collision-free Motion.....	69
3.7.3	Case Study 3: Implementation	74
3.8	Conclusion.....	76
Chapter 4	Effective Control Approach to Haptic Device-Robot Interface.....	77
4.1	Haptic Device Coordination System.....	78
4.2	Haptic Force Generation Method.....	80
4.2.1	Haptic Force Generation for a 3DOF Haptic Device.....	81
4.2.2	Haptic Force Generation for a 6DOF Haptic Device.....	83
4.3	Workspace Mapping Method	86
4.3.1	Workspace Transformation.....	87
4.3.2	Scaling Control	89
4.3.3	Drifting Control	90
4.3.4	Edge Motion Control	90
4.3.5	Experimental Testing	91
4.4	Determination of Parameters and Computation Time.....	93
4.4.1	Magnitudes of Repulsive Force and Attractive Force	94
4.4.2	Computational Time	97
4.4.3	Occupancy Voxel Indexing Approach.....	98
4.5	Implementation and Experimental Testing	100
4.5.1	System Setup for Implementation.....	100
4.5.2	Processing Time.....	103
4.5.3	Time Delay.....	105
4.5.4	Field Testing	112
4.6	Conclusion.....	115

Chapter 5 Human Factor Model for Haptic-based Human-Robot-Environment Interaction	116
5.1 Index of Performance	117
5.2 Determination of View Distance.....	119
5.2.1 Definition	119
5.2.2 Experimental Test Design.....	121
5.2.3 Results.....	123
5.2.4 Discussion	127
5.3 Extended Hand Movement Model	128
5.3.1 Pointing Accuracy.....	128
5.3.2 Experimental Test	130
5.3.3 Extended Hand Movement Model.....	146
5.4 Haptic Force-Speed Control Method	148
5.4.1 Test 1: Steering Test in a Simple 2D Environment	150
5.4.2 Test 2: Steering Test with a Robot Manipulator	158
5.4.3 Discussion	169
5.5 Conclusion.....	169
Chapter 6 Conclusion.....	171
6.1 Summary of Contributions	172
6.1.1 Three Dimensional Virtual Force Field Method.....	172
6.1.2 Attractive Force Method	172
6.1.3 Workspace Mapping Method.....	173
6.1.4 Extended Hand Movement Model	173
6.1.5 Haptic-based Human-Robot-Environment Interaction for Sandblasting Robotic System	173
6.2 Discussion and Future Work	174
Appendix A. Sandblasting Robotic System.....	176
Appendix B. Steering Test with Novint®Falcon Haptic Device.....	179

Appendix C. Table of Standard Normal Distribution..... 182

Bibliography 185

List of Figures

Figure 1.1 Examples of industrial applications in which operators can be replaced by a mobile robot manipulator to interact with complex environments in hazardous workplaces: (a) Sand blasting operation in steel bridge maintenance, (b) Vessel maintenance (from Broadbent's, Inc)	4
Figure 1.2 Prototype of the sandblasting robotic system	5
Figure 1.3 Human-Robot-Environment Interaction (HREI) diagram	7
Figure 2.1 a) A mobile robot with 3D scanner, b) 3D local map of a mine corridor, c) 3D virtualisation of a volumetric mine map [32][33]	15
Figure 2.2 Manipulator covered skin-type sensors [38][39][41]	16
Figure 2.3 (a) Various intermediate configurations (b) Path found between start (1) and goal (4) configurations [3]	17
Figure 2.4 (a) Probabilistic roadmaps [43] [44], (b) RRT method [46]	18
Figure 2.5 An example of a 2D potential field [5]: (a) Operational space of a robot, (b) Attractive potential field, (c) Artificial potential field, (d) Potential field	19
Figure 2.6 Elastic tunnel: configurations are selected from pre-planned path. The union of protective hulls of these configurations forms an elastic tunnel. [7]	20
Figure 2.7 (a) System overview of multipurpose robot for installing construction materials [56][57], (b) System overview of PowerMate robot for gearbox assembly [58]	22
Figure 2.8 Robot-dummy crash simulation setups [84]	25
Figure 2.9 Haptic force reflection (rearranged figure from [92])	26
Figure 2.10 Virtual spring conceptual diagram [96]	27
Figure 2.11 A model of the master-slave teleoperation system with computation time and communication delay time.	28
Figure 2.12 Common target patterns for performance testing of pointing tasks by Fitts's law	31

Figure 2.13 (a) Path width does not change, (b) Path width changes with path length	32
Figure 2.14 Control-Display scale and Control-Movement scale	33
Figure 3.1 (a) The Virtual Force Field (VF ²) approach that enables safe and efficient Robot-Environment Interaction (REI) (b) A sandblasting robotic system	37
Figure 3.2 Environmental mapping and surface material-type classification using laser scanner [34] a) shows an environment, and a manipulator affixed with a laser range finder at the end-effector, b) shows a 3D map of the environment represented as a point cloud.	39
Figure 3.3 a) Denso manipulator VM6083 (from www.aarobotics.co.uk) and sandblasting nozzle, b) Graphic model of the manipulator, and c) Geometry outline structure of the manipulator	41
Figure 3.4 An external force acting on a link of a manipulator and the position of the force	44
Figure 3.5 An example of attractive force at the end-effector of the extended manipulator	48
Figure 3.6 Graph of the amplitude of f_{att} with $K_{att} = 1$, $\epsilon_0 = 0.0001$, and different values of K_s	49
Figure 3.7 A single attractive force at the end-effector of the manipulator	49
Figure 3.8 Two attractive forces on the end-effector link of the manipulator	50
Figure 3.9 Three attractive forces at the end-effector link of the manipulator	52
Figure 3.10 Parameters of the ellipsoids D_{min} and D_{max} and a robot manipulator covered by D_{min}	54
Figure 3.11 A graph of the amplitude of repulsive force with $K_f=10$, $K_p=1.05$ and Er	56
Figure 3.12 D_{min} and D_{max} generated by sphere-swept bounding	57
Figure 3.13 Distance between two D_{min} s defined by sphere-swept bounding	61
Figure 3.14 Distance d_0 between D_{min} of a link and D_{min} of the mobile platform	62
Figure 3.15 Sandblasting a surface (ceiling) of a steel bridge structure	65
Figure 3.16 Joint angles of the manipulator tracking a path in Figure 3.15(a)	65
Figure 3.17 Snapshot of a manipulator performing a sandblasting task on an I-beam in a steel bridge maintenance environment	66
Figure 3.18 Joint angle changes of the manipulator following a pre-planned path shown in Figure 3.17(c)	66

Figure 3.19 (a) Manipulator spray-painting on a wall (b) Joint angle changes with a pre-planned path.....	67
Figure 3.20 (a) A manipulator spray-painting a cylinder ventilator, (b) Joint angle changes of the manipulator with a pre-planned path	67
Figure 3.21 A manipulator spray-painting a ceiling surface.....	68
Figure 3.22 Joint angle changes of the manipulator with a pre-planned path in Figure 3.21a.....	68
Figure 3.23 Block diagram of the VF ² approach for motion planning for a manipulator	69
Figure 3.24 A manipulator approaching multiple target positions (2), (3) and (4)	70
Figure 3.25 Joint angle changes of the manipulator approaching the target positions shown in Figure 3.24.....	71
Figure 3.26 A manipulator following a pre-planned path.....	72
Figure 3.27 (a) Speed of the end-effector at 75 mm/sec, (b) Speed of the end-effector at 35 mm/sec, (c) Speed of the end-effector at 15 mm/sec	72
Figure 3.28 (a) Orientation change at speed 15 mm/sec, (b) Orientation change at speed 35 mm/sec, (c) Orientation change at speed 75 mm/sec, and (d) Orientation angle difference at different speeds	73
Figure 3.29 Pre-planned path for a sandblasting robotic system	74
Figure 3.30 Snapshot of implementation in a sandblasting robot system.....	75
Figure 4.1 Haptic device-robot interface	77
Figure 4.2 A 3DOF haptic device: Novint® Falcon.....	78
Figure 4.3 A 6DOF haptic device: Phantom® Omni	79
Figure 4.4 Block diagram of haptic-based interaction.....	80
Figure 4.5 Attractive force and haptic force for a 3DOF haptic device	81
Figure 4.6 Control orientation of the end-effector link by a 3DOF haptic device.....	82
Figure 4.7 Attractive force and virtual spring when a 6DOF haptic device is used	83
Figure 4.8 Multiple attractive forces to control the target point, the target orientation and the length of the blasting stream	85
Figure 4.9 Haptic Coordinate System, Camera (operator view) Coordinate System, and Manipulator Coordinate System	87
Figure 4.10 Control diagram of workspace mapping	88

Figure 4.11 Haptic workspace mapping: a) Up scaling and drifting, b) Drifting when haptic workspace is in maximum, c) Drifting when the cursor is on the edge of the haptic workspace, d) Down scaling and drifting when the cursor is stopped.....91

Figure 4.12 Snapshots of a simulation test to validate the workspace mapping method.92

Figure 4.13 Speed of the haptic cursor in the simulation test shown in Figure 4.12...93

Figure 4.14 Attractive force estimated by a linear function of a virtual spring.....95

Figure 4.15 Two case studies: (a) the manipulator cannot move to penetrate obstacles such as walls, (b) the manipulator breaks through the wall when the K_f does not satisfy the constraint of Equation 4.36.....97

Figure 4.16 Computation time with respect to the number of points in the point cloud set of an environment.....98

Figure 4.17 Occupancy voxel map of a link of manipulator 100

Figure 4.18 (a) A virtual environment,(b) The sandblasting robotic system under a mock-up steel-bridge structure 101

Figure 4.19 Snapshots of the first implementation with haptic device interface..... 102

Figure 4.20 Timing diagram of the open-loop control and closed-loop control..... 103

Figure 4.21 a) A testing plan, b) The manipulator movement in this experiment..... 104

Figure 4.22 The manipulator's joint angles in open-loop control at 25% of maximum speed of the manipulator, indicated by dash lines for the virtual manipulator and solid lines for the actual manipulator..... 106

Figure 4.23 Time delay at 25% of the maximum speed in open-loop control from Figure 4.22 106

Figure 4.24 Haptic force in the test at 25% of the maximum speed with open-loop control 107

Figure 4.25 The manipulator's joint angles obtained from open-loop control at 50% of the maximum speed of the manipulator: dash lines for virtual manipulator and solid lines for actual manipulator 108

Figure 4.26 Time delay at 50% of the maximum speed in open-loop control from Figure 4.25 108

Figure 4.27 Haptic force in the test at 50% of the maximum speed with open-loop control 108

Figure 4.28 The manipulator’s joint angles obtained from closed-loop control at 25% of the maximum speed of the manipulator, indicated by dash lines for the virtual manipulator and solid lines for the actual manipulator..... 109

Figure 4.29 Haptic force in the test at 25% of the maximum speed with closed-loop control 110

Figure 4.30 The manipulator’s joint angles obtained from closed-loop control at 50% of the maximum speed of the manipulator, indicated by dash lines for the virtual manipulator and solid lines for the actual manipulator..... 111

Figure 4.31 Haptic force in the test at 50% of the maximum speed with closed-loop control 111

Figure 4.32 Virtual environment of a steel bridge channel section in the field test .. 112

Figure 4.33 Snapshots of the field test: the manipulator performs a dry run sandblasting..... 113

Figure 4.34 Haptic force along the trajectory of the manipulator..... 114

Figure 4.35 (a) Amplitude of the haptic force shown in Figure 4.34 (b) Speed of the end-effector of the manipulator along the path shown in Figure 4.34..... 114

Figure 5.1 Example of human factors affecting Human-Robot-Environment Interaction (HREI) 116

Figure 5.2 Error distribution 118

Figure 5.3 Object-to-screen projection 120

Figure 5.4 Setup of the robot steering test with different view distances (d_v); (a) Image of view distance at $d_v=2m$, (b) Image of view distance at $d_v=6m$, and (c) Diagram of the camera’s position 122

Figure 5.5 *IP* of the 6 participants are shown as red points and the Average *IP* of the 6 participants are shown in black lines. 127

Figure 5.6 Pointing accuracy at 4σ of point-to-point task and path tracking task 129

Figure 5.7 Pointing accuracy testing diagram..... 131

Figure 5.8 Coordinate transformation..... 132

Figure 5.9 Pointing accuracy experiment setup 133

Figure 5.10 Force calibration of a haptic device (Novint® Falcon)..... 134

Figure 5.11 Haptic force measured from the eight participants with 3 different stiffness properties: (a) when the virtual spring stiffness is 0.78kgf/m; (b) when the virtual spring stiffness is 1.56 kgf/m, and (c) when the virtual spring stiffness is 2.33 kgf/m..... 135

Figure 5.12 Distribution of the haptic cursor position: Results from the 1st participant	137
Figure 5.13 Distribution of the haptic cursor position: Results from the 2nd participant	138
Figure 5.14 Distribution of the haptic cursor position: Results from the 3rd participant	139
Figure 5.15 Distribution of the haptic cursor position: Results from the 4th participant	140
Figure 5.16 Distribution of the haptic cursor position: Results from the 5th participant	141
Figure 5.17 Distribution of the haptic cursor position: Results from the 6th participant	142
Figure 5.18 Distribution of the haptic cursor position: Results from the 7th participant	143
Figure 5.19 Distribution of the haptic cursor position: Results from the 8th participant	144
Figure 5.20 Average of standard deviation of all participants	145
Figure 5.21 Haptic force-cursor speed (m/s) graph with different pointing accuracy, $\sigma = 12.7\text{mm}$.	147
Figure 5.22 (a) Control diagram of haptic based interaction without HFSC, (b) Control diagram of haptic based interaction with HFSC	149
Figure 5.23 Steering test in a simple 2D environment	150
Figure 5.24 Results of steering test with 15.9mm track width and low resistant force (level 1); standard deviations (σ) are 2.2mm and 1.5mm for tests with (green) and without (red) the HFSC method.	152
Figure 5.25 Results of steering test with 12.7mm track width and low resistant force (level 1); standard deviation (σ) are 1.8mm and 1.3mm for tests with (green) and without (red) the HFSC method.	152
Figure 5.26 Results of steering test with 9.53mm track width and low resistant force (level 1); standard deviation (σ) are 1.4mm and 0.8mm for tests with (green) and without (red) the HFSC method.	153

Figure 5.27 Results of steering test with 6.35mm track width and low resistant force (level 1); standard deviation (σ) are 1.1mm and 0.8mm for tests with (green) and without (red) the HFSC method.....	153
Figure 5.28 Results of steering test with 15.9mm track width and high resistant force (level 2); standard deviation (σ) are 1.3mm and 1.0mm for tests with (green) and without (red) the HFSC method.....	154
Figure 5.29 Results of steering test with 12.7mm track width and high resistant force (level 2); standard deviation (σ) are 2.1mm and 1.0mm for tests with (green) and without (red) the HFSC method.....	154
Figure 5.30 Results of steering test with 9.53mm track width and high resistant force (level 2); standard deviation (σ) are 1.3mm and 0.9mm for tests with (green) and without (red) the HFSC method.....	155
Figure 5.31 Results of steering test with 6.35mm track width and high resistant force (level 2); standard deviation (σ) are 1.0mm and 0.8mm for tests with (green) and without (red) the HFSC method.....	155
Figure 5.32 Index of performance with different resistance force, (a) at low resistant force (level 1), (b) high resistant force (level 2)	157
Figure 5.33 Test setup.....	158
Figure 5.34 Results of steering test with a robot manipulator: low level resistant force (level 1) and 20mm track width. Left: haptic force - end-effector speed data; top right: end-effector position during the experiment without the HFSC method; bottom right: end-effector position during the experiment with the HFSC method.....	160
Figure 5.35 Results of steering test with a robot manipulator: low level resistant force (level 1) and 40mm track width. Left: haptic force - end-effector speed data; top right: end-effector position during the experiment without the HFSC method; bottom right: end-effector position during the experiment with the HFSC method.....	161
Figure 5.36 Results of steering test with a robot manipulator: low level resistant force (level 1) and 60mm track width. Left: haptic force - end-effector speed data; top right: end-effector position during the experiment without the HFSC method; bottom right: end-effector position during the experiment with the HFSC method.....	161
Figure 5.37 Results of steering test with a robot manipulator: low level resistant force (level 1) and 80mm track width. Left: haptic force - end-effector speed data; top right:	

end-effector position during the experiment without the HFSC method; bottom right:
end-effector position during the experiment with the HFSC method..... 162

Figure 5.38 Results of steering test with a robot manipulator: medium level resistant
force (level 2) and 20mm track width. Left: haptic force - end-effector speed data; top
right: end-effector position during the experiment without the HFSC method; bottom
right: end-effector position during the experiment with the HFSC method 162

Figure 5.39 Results of steering test with a robot manipulator: medium level resistant
force (level 2) and 40mm track width. Left: haptic force - end-effector speed data; top
right: end-effector position during the experiment without the HFSC method; bottom
right: end-effector position during the experiment with the HFSC method 163

Figure 5.40 Results of steering test with a robot manipulator: medium level resistant
force (level 2) and 60mm track width. Left: haptic force - end-effector speed data; top
right: end-effector position during the experiment without the HFSC method; bottom
right: end-effector position during the experiment with the HFSC method 163

Figure 5.41 Results of steering test with a robot manipulator: medium level resistant
force (level 2) and 80mm track width. Left: haptic force - end-effector speed data; top
right: end-effector position during the experiment without the HFSC method; bottom
right: end-effector position during the experiment with the HFSC method 164

Figure 5.42 Results of steering test with a robot manipulator: high level resistant force
(level 3) and 20mm track width. Left: haptic force - end-effector speed data; top right:
end-effector position during the experiment without the HFSC method; bottom right:
end-effector position during the experiment with the HFSC method..... 164

Figure 5.43 Results of steering test with a robot manipulator: high level resistant force
(level 3) and 40mm track width. Left: haptic force - end-effector speed data; top right:
end-effector position during the experiment without the HFSC method; bottom right:
end-effector position during the experiment with the HFSC method..... 165

Figure 5.44 Results of steering test with a robot manipulator: high level resistant force
(level 3) and 60mm track width. Left: haptic force - end-effector speed data; top right:
end-effector position during the experiment without the HFSC method; bottom right:
end-effector position during the experiment with the HFSC method..... 165

Figure 5.45 Results of steering test with a robot manipulator: high level resistant force
(level 3) and 80mm track width. Left: haptic force - end-effector speed data; top right:
end-effector position during the experiment without the HFSC method; bottom right:
end-effector position during the experiment with the HFSC method..... 166

Figure 5.46 Index of performance with path-track width 168

Figure A.1 Robot and Platform Controller Diagram 177

Figure A.2 A laser scanner (Left), an example environmental map (Right) 178

Figure A.3 A Sandblasting System, (a) A system for small-scale blasting using
blasting gun, (b) A system for industrial scale blasting 178

Figure B.1 Hand movement testing in circular path track (unit: m) 179

Figure B.2 Hand movement testing result of 4 participants 180

Nomenclature

General Formatting Style

$f(\dots)$	A scalar valued function	
$\mathbf{f}(\dots)$	A vector function	
$\mathbf{F}(\dots)$	A matrix function	
$\{\dots\}$	A set of ...	
$[\dots]^T$	Transpose	
$ \dots $	Absolute value	
$\ \dots\ $	Vector length	
$\min\min\{\dots\}$	The objective function of two parameters minimization	
$\prod \dots$	Product sign	
x	A scalar variable	- lower case and italic
X	A scalar variable	-upper case and italic
\mathbf{x}	A vector or a single-dimensional matrix	- lower case and bold
\mathbf{X}	A matrix or a set	- upper case and bold
$P(Z \leq a)$	Cumulative probability function	
$P(Z \geq a)$	Complementary cumulative probability function	
$P(b \leq Z \leq a)$	Cumulative point-to-point probability function	

General Referencing with Subscript and Superscript

${}^{\dots}x_{\dots}$	A scalar variable	
	-	Front superscript is reference coordinate

- Rear subscript is transforming coordinate

${}^{\dots}x_{\dots}$ A scalar variable

- Front superscript is reference coordinate
- Rear first subscript is numerical index, customized abbreviation or description
- Rear second subscript is transforming coordinate

${}^{\dots}X_{\dots}$ or ${}^{\dots}x_{\dots}$ A matrix

- Front superscript is reference coordinate
- Rear subscript is transforming coordinate

${}^{\dots}X_{\dots}$ or ${}^{\dots}x_{\dots}$ A matrix

- Front superscript is reference coordinate
- Rear first subscript is numerical index, customized abbreviation or description
- Rear second subscript is transforming coordinate

X_{\dots} A set (does not have front superscript)

- Rear first subscript is customized abbreviation or description
- Rear second subscript is index of set's member

Local and Global Variables

i,j Index of a set or to refer to a count

x,y,z Axes of Cartesian coordinate

\mathfrak{R}^3 3DOF Cartesian space

\mathfrak{R}^6 6DOF Cartesian space

\mathfrak{R}_q^7 7DOF manipulator's joint space

Specific Symbol Usage

${}^{...}\mathbf{T}_{...}$	A homogeneous transformation matrix (4 by 4)
${}^{...}\mathbf{R}_{...}$	A rotation matrix (3 by 3)
${}^{...}\mathbf{n}_{...}$	A directional vector or a normal vector (3 by 1)
${}^{...}\mathbf{p}_{...}$	A position vector (3 by 1)
${}^{...}\mathbf{P}_{...}$	A configuration vector (6 by 1), a combination of $[{}^{...}\mathbf{n}_{...}, {}^{...}\mathbf{p}_{...}]$
n_x, n_y, n_z	components of ${}^{...}\mathbf{n}_{...}$
p_x, p_y, p_z	components of ${}^{...}\mathbf{p}_{...}$

$\mathbf{F}_{...}$	A 6DOF spatial force
$\mathbf{f}_{...}$	A 3DOF linear force, a component of $\mathbf{F}_{...}$
$\boldsymbol{\sigma}_{...}$	A 3DOF angular moment, a component of $\mathbf{F}_{...}$
$f_{...x}, f_{...y}, f_{...z}$	scalar components of $\mathbf{f}_{...}$
$\sigma_{...x}, \sigma_{...y}, \sigma_{...z}$	scalar components of $\boldsymbol{\sigma}_{...}$

\mathbf{q}	A joint position matrix (7 by 1)
q_i	A position of joint i , a component in \mathbf{q} <ul style="list-style-type: none"> - joint 1 to 6 are angle (degree) - joint 7 is length (m)

\mathbf{I}	Mass-inertia matrix of the robot links
$\boldsymbol{\beta}$	Damping coefficient matrix of the robot joints
$\boldsymbol{\kappa}$	Stiffness coefficient matrix of the robot joints

$\boldsymbol{\Gamma}$	A torque-force matrix defining in joint space (7 by 1)
τ_i	Joint torque-force of a joint i , a component in $\boldsymbol{\Gamma}$ <ul style="list-style-type: none"> - joint 1 to 6 are torque (N.m) - joint 7 is linear force (N)

$\boldsymbol{\Gamma}_{att}$	Attractive torque-force matrix
$\boldsymbol{\Gamma}_{rep_i}$	Repulsive torque-force matrix on a link in joint i coordinate

${}^0\mathbf{P}_e$	Configuration of the end-effector of a manipulator
${}^0\mathbf{n}_e$	A component of ${}^0\mathbf{P}_e$
${}^0\mathbf{p}_e$	A component of ${}^0\mathbf{P}_e$
${}^0\mathbf{P}_t$	Configuration of target/attractive point for the manipulator's end-effector
${}^0\mathbf{n}_t$	A component of ${}^0\mathbf{P}_t$
${}^0\mathbf{p}_t$	A component of ${}^0\mathbf{P}_t$
\mathbf{F}_{att}	A6DOF spatial attractive force for the manipulator's end-effector
\mathbf{f}_{att}	A 3DOF attractive force (linear force), a component of \mathbf{F}_{att}
$\boldsymbol{\sigma}_{att}$	A 3DOF attractive moment (angular moment), a component of \mathbf{F}_{att}
$f_{att\ x}, f_{att\ y}, f_{att\ z}$	components of \mathbf{f}_{att}
$\sigma_{att\ x}, \sigma_{att\ y}, \sigma_{att\ z}$	components of $\boldsymbol{\sigma}_{att}$
$K_{att\ 1}$	Coefficient of a linear attractive force's amplitude
$K_{att\ 2}$	Coefficient of an angular attractive moment's amplitude
ε_0	A small non-zero positive constant (in this research $\varepsilon_0=0.0001$)
K_{as}	A constant for defining a transient state of the attractive force
δ_a	Attractive force function
\mathbf{P}_{ob}	Obstacle point cloud set
${}^0\mathbf{p}_{ob\ i}$	The i^{th} member in the obstacle point cloud set
m	Number of points in the obstacle point cloud set
D_{min}	inner force field
D_{max}	outer force field
Er	distance between D_{min} and D_{max}
r_c	The radius of D_{min}
${}^0\mathbf{p}1_i$	Ending point 1 of the centre line of a link in joint i coordinate

${}^0\mathbf{p}2_i$	Ending point 2 of the centre line of a link in joint i coordinate
${}^0\mathbf{p}3_i$	The nearest point on the centre line of a link on joint i coordinate
u	A parameter of a centre line of a link function for defining ${}^0\mathbf{p}3_i$
${}^0\mathbf{p}_{ob_s}$	The point in the point cloud set that is the closest point to a manipulator link at ${}^0\mathbf{p}3_i$
ds_s	The shortest distance measured from ${}^0\mathbf{p}_{ob_s}$ to ${}^0\mathbf{p}3_i$
d_0	The shortest distance from the point ${}^0\mathbf{p}_{ob_s}$ to the surface of D_{min}
\mathbf{F}_{rep_i}	A spatial repulsive force on a link of a manipulator in joint i coordinate
\mathbf{f}_{rep_i}	A repulsive force on a link of a manipulator in joint i coordinate, a component of \mathbf{F}_{rep_i}
$f_{rep_{x_i}}, f_{rep_{y_i}}, f_{rep_{z_i}}$	components of \mathbf{f}_{rep_i}
δ_r	Repulsive force function
K_f	A coefficient of the amplitude of a repulsive force
\mathbf{H}_i	Force transformation matrix in joint i coordinate
${}^0\mathbf{p}_f$	Position vector of a force
\mathbf{h}_j	j^{th} component of \mathbf{H}
\mathbf{L}_i	Configuration matrix of joint i coordinate
\mathbf{M}_{\dots}	A rotation skew-symmetric matrix (6 by 6)
$\mathbf{S}(\Delta\mathbf{p})$	A skew-symmetric matrix (3 by 3)
$\Delta\mathbf{p}$	A differential vector between ${}^0\mathbf{p}_i$ and ${}^0\mathbf{p}_f$
$\Delta p_x, \Delta p_y, \Delta p_z$	components of $\Delta\mathbf{p}$
\mathbf{F}_h	A haptic force
k_{vir}	Coefficient of virtual spring stiffness

${}^0 \mathbf{p}_a$	Position vector of the haptic cursor on the world coordinate
${}^0 \mathbf{p}_h$	Position vector of the haptic cursor on the haptic workspace coordinate
${}^0 \mathbf{p}_w$	Position vector of the haptic workspace origin on the world coordinate
${}^0 \dot{\mathbf{p}}_h$	Velocity vector of the haptic cursor on the haptic workspace coordinate
${}^0 \dot{\mathbf{p}}_w$	Drifting velocity of the haptic workspace origin on the world coordinate

k_{sc}	Workspace scaling coefficient
\dot{k}_{sc}	Workspace scaling rate (first order differentiate)
k_{sp}	Positive scaling rate of scaling control
k_{sn}	Negative scaling rate of scaling control
k_{dp}	The positive drifting rate of drifting control
k_{em}	Drifting rate of edge motion control
v_{ht}	Haptic cursor speed threshold

k_e	Elasticity coefficient of a 3D-VF ² (virtual skin)
μ_{cap}	Energy absorbability of a 3D-VF ²
μ_{in}	Potential energy from the attractive force

φ	Probability density
O_{acc}	Pointing accuracy
Z_{ac}	Coefficient of the pointing accuracy
σ	Standard deviation of robot end-effector in a pointing task
σ^2	Variance of robot end-effector in a pointing task
IP	Index of Performance

\emptyset	Path-track width
\emptyset_{obj}	Dimension of a task plane
\emptyset_{scn}	Dimension of a computer screen
d_v	A view distance between a camera screen and an object plane

α_v	A camera's field of view
G_e	A control display scale
G_h	A control movement scale
G_x	A control scale
MT	Hand movement time
a	Operator's start/stop movement time
b	Operator's hand movement speed
v_a	A haptic cursor speed from hand movement model
k_{pw}	Coefficient of power expense in haptic interface